Midlatitude–Equatorial Dynamics of a Grounded Deep Western Boundary Current. Part II: Cross-Equatorial Dynamics

GORDON E. SWATERS

Institute of Applied Mathematics, Department of Mathematical and Statistical Sciences, and Institute for Geophysical Research, University of Alberta, Edmonton, Alberta, Canada

(Manuscript received 15 October 2014, in final form 22 May 2015)

ABSTRACT

This is Part II of a two-part theoretical study into the midlatitude–cross-equatorial dynamics of a deep western boundary current (DWBC) in an idealized meridionally aligned, differentially rotating ocean basin with zonally varying parabolic bottom topography. Part I determined the midlatitude flow across the planetary vorticity gradient and the dynamics of the DWBC as it begins to enter the equatorial region in the ''intermediate equatorial region.'' Part II determines the nonlinear dynamics of the DWBC as it flows across the basin along the equator in the ''inner equatorial region.'' The large-scale structure of the flow within the inner equatorial region corresponds to a zonally aligned nonlinear stationary planetary wave pattern that meanders about the equator in which the flow exits the equatorial region on the eastern side of the basin. In addition to numerically determining the pathlines for the large-scale equatorial flow, an approximate nonlinear model is introduced for which an analytical solution can be obtained for the nonlinear planetary wave along the equator. If the DWBC exits the equatorial region into the opposite hemisphere from its source hemisphere, the characteristic curves associated with the flow must necessarily intersect within the inner equatorial region. It is in the regions of intersecting characteristics that dissipation makes a leading-order contribution to the dynamics and induces the requisite potential vorticity adjustment permitting the cross-equatorial flow of a DWBC that is in planetary geostrophic dynamical balance in midlatitudes.

1. Introduction

This paper is Part II of a two-part theoretical study of the midlatitude–cross-equatorial dynamics of deep western boundary currents (DWBCs) in an idealized differentially rotating meridional basin with parabolic bottom topography (so that the ocean basin shallows on the both the eastern and western sides).

In Swaters (2015, hereinafter Part I) we were able to explicitly solve the leading-order steady-state equations for the nonlinear midlatitude flow along the western sloping boundary and across the planetary vorticity gradient for a grounded DWBC that possesses distinct upslope and downslope groundings or incroppings in the DWBC height or thickness (see Figs. 1 and 2a in Part I). The midlatitude DWBC solution found in Part I was found to speed up and the height to decrease as the equator was approached (while maintaining constant meridional volume transport). The structure of the midlatitude solution suggested the emergence of an ''intermediate'' equatorial inertial boundary layer centered on the equator with a scale meridional width on the order of 885 km where the nonlinear terms in the momentum equations begin to make an order one contribution to the dynamics. The leading-order equations associated with the ''intermediate'' equatorial inertial boundary layer could be solved exactly. The solution for the idealized DWBC was found to turn eastward, forming a zonally aligned equatorial jet. However, it was found that the solution in the intermediate region continues to speed up and the DWBC height continues to decrease as the equator is approached. This suggests the emergence of an ''inner'' equatorial inertial boundary layer in which the flow becomes fully nonlinear and where the velocities are finite and the DWBC height is nonzero.

The principal purpose of Part II is to describe of the dynamics of the DWBC in this ''inner'' equatorial inertial boundary layer. In particular, we show that the inner inertial region corresponds to a narrow zonal band

Corresponding author address: Gordon E. Swaters, Department of Mathematical and Statistical Sciences, University of Alberta, 632 Central Academic Building, Edmonton AB T6G2G1, Canada. E-mail: gswaters@ualberta.ca

DOI: 10.1175/JPO-D-14-0208.1

of meridional width on the order of 221 km centered along the equator. Within this inner region, the leading-order momentum equations are fully nonlinear but do not contain the pressure gradient terms associated with the DWBC height. To leading order, it is the downslope gravitational acceleration associated with a grounded water mass sited on a sloping bottom (on an equatorial β plane) that drives the dynamics in the momentum equations and thereby determines the velocity field in the DWBC. The DWBC height or thickness is determined by mass or volume transport conservation or, alternatively, by potential vorticity (PV) conservation. The solution for the inner inertial boundary layer equations can be solved using the method of characteristics for which we present solutions for the pathlines or Lagrangian trajectories (and the Eulerian velocities). The equatorial pathlines in the inner equatorial region correspond to a predominately zonal jet that meanders meridionally as the DWBC flows eastward. The "wavelength" of these meanders is computed to be about 1830 km. Given the high degree of uncertainty, this estimate is not inconsistent with the observations described in Part I. These meanders are an intrinsically nonlinear stationary planetary wave that develops as the DWBC first "overshoots" the equator in the western side of the basin, with PV conservation on an equatorial β plane subsequently attempting to rectify the flow. We are able to, under a suitable approximation, to find an analytical solution for these abyssal equatorial meanders, which has not appeared in the literature before.

The inertial inner equatorial region model we introduce here for the DWBC conserves energy along the pathlines. Thus, as the grounded DWBC flows eastward, it eventually encounters the basin shallowing on the eastern side. As the grounded DWBC flows upward along the boundary on the eastern side, its potential energy increases to the point that eventually energy conservation halts the upslope motion and the DWBC must exit the equatorial region and begin to flow along isobaths on the sloping boundary on the eastern side. Whether the DWBC current exits the equatorial region and flows back into the Northern Hemisphere or crosses the equator and flows into the Southern Hemisphere is determined by the point in the phase of the stationary planetary wave that the flow is in at the point of maximum upslope position (see Kim et al. 2014). For parameter values consistent with the geometry of the Atlantic Ocean, our model predicts that DWBC exits completely into the Southern Hemisphere.

In addition, it is shown that there must always be at least one region within the stationary equatorial wave that the characteristics or pathlines intersect if there is to be genuine sustained cross-equatorial flow (i.e., if the DWBC current exits the equatorial region into the Southern Hemisphere and continues to flow southward along the eastern topographic slope). The regions of intersecting characteristics or pathlines are locations where the velocity gradients become very large, and these are precisely the locations where dissipation cannot be neglected (and in fact must occur; e.g., Edwards and Pedlosky 1998a,b) in the dynamics. The theory presented here suggests that the dissipation regions are meridionally quite narrow and zonally constrained with a zonal length scale of about 165 km and a meridional width on the order of 11 km and are located near the crest and troughs of the stationary planetary equatorial wave.

The plan of Part II is as follows. In section 2, the leading-order equations for the inner equatorial inertial boundary layer are introduced. These are reduced to a set of nonlinear characteristic equations that are solved numerically. The basin-scale structure of the inner equatorial region solution is described, as is the structure of the solution in the region where the characteristics nominally intersect. In section 3, we describe an approximate model for the nonlinear stationary planetary equatorial wave that can be explicitly solved. The paper is summarized in section 4.

2. The inner equatorial region

Our notation here, which is for the most part quite standard, is identical to that used in Part I, and the reader is referred to Part I for complete details. Part I concludes with the determination of the dynamics of the DWBC as it enters the equatorial region in what we called the "intermediate inertial equatorial boundary layer," which has a meridional width, centered on the equator, of about $O(\varepsilon^{1/3}R) \simeq 885$ km, where $\varepsilon \simeq 2.6 \times 10^{-3}$ is the Rossby number and R is the radius of the Earth [see (13) in Part I]. After introducing a rescaling for the meridional coordinate and the velocities [see (59) in Part I] appropriate for the dynamics in the intermediate layer, the reduced-gravity shallow water equations (with horizontal dissipation included) in the intermediate region can be written in the form [see (60)–(62) in Part I]

$$\kappa^2(\varepsilon^{1/3}\tilde{u}\partial_x + \tilde{v}\partial_\xi)\tilde{u} - \frac{\sin(\varepsilon^{1/3}\xi)}{\varepsilon^{1/3}}\tilde{v} = -(h_B + \varepsilon^{1/3}\tilde{h})_x + \frac{1}{\mathrm{Re}}(\varepsilon^{2/3}\partial_{xx} + \kappa^2\partial_{\xi\xi})\tilde{u}, \quad (1)$$

$$\varepsilon^{1/3}\tilde{u}\tilde{v}_x + \tilde{v}\tilde{v}_\xi + \frac{\sin(\varepsilon^{1/3}\xi)}{\varepsilon^{1/3}}\tilde{u} = -\tilde{h}_\xi + \frac{1}{\kappa^2\mathrm{Re}}(\varepsilon^{2/3}\partial_{xx} + \kappa^2\partial_{\xi\xi})\tilde{v}, \quad \text{and} \quad (2)$$

$$\varepsilon^{1/3}(\tilde{u}\tilde{h})_x + (\tilde{v}\tilde{h})_\xi = 0, \quad (3)$$

where $\kappa \simeq 1.6 \times 10^{-2}$ is the aspect ratio between the zonal and meridional lengths scales in midlatitudes; Re = 2464 is the Reynolds number [see (16) in Part I], $\tilde{u}$ and $\tilde{v}$ are the scaled zonal and meridional velocities [see (59) in Part I]; and x and ξ are the nondimensional midlatitude zonal coordinate [see (7) in Part I] and the scaled "intermediate region" meridional coordinate [see (59) in Part I], respectively. As pointed out in Part I, it is noted that

$$O(\varepsilon^2) \lesssim \kappa^2 \simeq \mathrm{Re}^{-1} \lesssim O(\varepsilon).$$

As shown in Part I, the intermediate region relations (1)–(3) have the leading-order solutions (valid in the limit $0 < \varepsilon \ll 1$) given by

$$\tilde{u} = \frac{1}{\xi}\left\{\frac{[h_B'(x)]^2}{\xi^3} - \frac{h_0[\tilde{\tau}(x)]}{\sin y_0}\right\}, \quad \tilde{v} = \frac{h_B'(x)}{\xi}, \quad \tilde{h} = \frac{\xi h_0[\tilde{\tau}(x)]}{\sin y_0},$$

where $\tilde{\tau}(x)$ is given by (53) in Part I, h_0 is the height or thickness of the DWBC associated with the midlatitude boundary condition along $y = y_0$ [see (11) in Part I], and h_B' is the eastward slope of the bottom topography given by (12) in Part I. These solutions will asymptotically match the midlatitude solutions obtained in Part I [see (26)–(29) in Part I] as the midlatitude meridional coordinate $y \to 0$ [see (54)–(56) in Part I]. The intermediate region solutions have the property that the DWBC turns eastward and forms an equatorial jet as ξ decreases toward zero (see Fig. 7c in Part I). In addition, we see that these solutions possess the property that $\tilde{h} \simeq O(\xi)$, $\tilde{u} \simeq O(\xi^{-4})$, and $|\tilde{v}| \simeq O(\xi^{-1})$ as the equator is approached, that is, as $\xi \to 0$. This unphysical and mathematically singular behavior suggests the emergence of an inner inertial equatorial boundary layer in which the inviscid dynamics is finally resolved, that is, the DWBC height does not go to zero and the velocities remain finite as the equator is approached.

In consideration of the above behavior in the intermediate region solutions, examination of (1) and (2) suggests that the Coriolis term in (1) remains $O(1)$ and that the meridional momentum flux term $\tilde{v}\tilde{v}_\xi$ remains balanced against the Coriolis term in (2) as $\xi \to 0$. Consequently, the next distinguished limit in (1) and (2) as $\xi \to 0$ occurs when the meridional flux term $\kappa^2\tilde{v}\tilde{u}_\xi$ in (1) becomes $O(1)$, that is, balances the Coriolis term, and when the zonal momentum flux term $\varepsilon^{1/3}\tilde{u}\tilde{v}_x$ balances the meridional momentum flux $\tilde{v}\tilde{v}_\xi$ and the Coriolis terms in (2). Both these balances occur when $\xi \simeq O(\kappa^{1/3})$ or, dimensionally, in a zonal band with meridional width on the order of $(\kappa\varepsilon)^{1/3}R \simeq 221$ km centered along the equator.

To this end we introduce the "inner" (careted) equatorial variables given by

$$\tilde{u} = \kappa^{-4/3}\hat{u}(x,\zeta), \quad \tilde{v} = \kappa^{-1/3}\hat{v}(x,\zeta),$$
$$\tilde{h} = \kappa^{1/3}\hat{h}(x,\zeta) \quad \text{and} \quad \xi = \kappa^{1/3}\zeta, \tag{4}$$

into (1), (2) and (3), yielding

$$\nu\hat{u}\hat{u}_x + \hat{v}\hat{u}_\zeta - \frac{\sin[(\kappa\varepsilon)^{1/3}\zeta]}{(\kappa\varepsilon)^{1/3}}\hat{v} = -[h_B + (\kappa\varepsilon)^{1/3}\hat{h}]_x + \frac{1}{\mathrm{Re}}(\nu^2\partial_{xx} + \partial_{\zeta\zeta})\hat{u}, \tag{5}$$

$$\nu\hat{u}\hat{v}_x + \hat{v}\hat{v}_\zeta + \frac{\sin[(\kappa\varepsilon)^{1/3}\zeta]}{(\kappa\varepsilon)^{1/3}}\hat{u} = -\kappa\hat{h}_\zeta + \frac{1}{\mathrm{Re}}(\nu^2\partial_{xx} + \partial_{\zeta\zeta})\hat{v}, \tag{6}$$

and

$$\nu(\hat{u}\hat{h})_x + (\hat{v}\hat{h})_\zeta = 0, \tag{7}$$

where $\nu \equiv (\varepsilon/\kappa^2)^{1/3} \simeq 2.21 \simeq O(1)$.

Within the context $\kappa^2 \simeq \mathrm{Re}^{-1} \lesssim O(\varepsilon)$, it follows that the leading-order problem (as $\varepsilon \to 0$) associated with (5)–(7) will be the equatorial β-plane balance given by the quasi-linear hyperbolic system of equations

$$(\nu\hat{u}\partial_x + \hat{v}\partial_\zeta)\hat{u} - \zeta\hat{v} = -h_B'(x), \tag{8}$$

$$(\nu\hat{u}\partial_x + \hat{v}\partial_\zeta)\hat{v} + \zeta\hat{u} = 0, \quad \text{and} \tag{9}$$

$$\nu(\hat{u}\hat{h})_x + (\hat{v}\hat{h})_\zeta = 0, \tag{10}$$

which must be solved subject to the asymptotic matching conditions

$$\hat{h} \to \frac{\zeta h_0[\tilde{\tau}(x)]}{\sin y_0}, \tag{11}$$

$$\hat{u} \to \frac{[h_B'(x)]^2}{\zeta^4}, \quad \text{and} \tag{12}$$

$$\hat{v} \to \frac{h_B'(x)}{\zeta}, \tag{13}$$

as $\zeta \to \infty$ (in the Northern Hemisphere, $\zeta \to -\infty$ in the Southern Hemisphere), where (11)–(13) are the leading-order behavior of the intermediate region solutions as $\xi \to 0$ written in the inner variables [(4)]. Again, it is noted that even though the matching conditions of (12) and (13) do not make explicit reference to $h_0[\tilde{\tau}(x)]$, it is understood that the solutions for $\hat{u}$ and $\hat{v}$ only have physical meaning in the context that $\hat{h} > 0$.

Observe that $\hat{h}$ does not appear in the leading-order momentum equations [(8) and (9)]. In the inner region, the solutions for $\hat{u}$ and $\hat{v}$ are no longer coupled to the

solution for $\hat{h}$, and the solution for $\hat{h}$ is obtained ''diagnostically'' from (10) given $\hat{u}$ and $\hat{v}$. That is, the pathlines of the flow in the inner equatorial region are no longer connected to the pressure gradient associated with the DWBC height and are solely determined by the gravitational acceleration/deceleration associated with the sloping bottom topography. Consequently, we expect that, roughly speaking, the steady flow will zonally accelerate in the western ''downslope'' portion of the bottom topography and will zonally decelerate in the eastern ''upslope'' portion of the bottom topography. We expect this deceleration to continue until the zonal velocity is zero, at which point the maximum eastward point is reached by the current after which it will reestablish itself as a, more or less, along-slope flowing grounded abyssal current.

The PV equation associated with (8)–(10), obtained by computing $\nu\partial_x(9) - \partial_y(8)$ and using (10), will be given by

$$(\nu\hat{u}\partial_x + \hat{v}\partial_\zeta)\left(\frac{\nu\hat{v}_x - \hat{u}_\zeta + \zeta}{\hat{h}}\right) = 0. \tag{14}$$

a. *The characteristic equations associated with the inner equatorial region*

The momentum equations [(8) and (9)] is a 2×2 system of quasi-linear hyperbolic equations that can be solved using the method of characteristics. The characteristic equations can be written in the form

$$\frac{dx}{d\sigma} = \nu\hat{u}, \tag{15}$$

$$\frac{d\zeta}{d\sigma} = \hat{v}, \tag{16}$$

$$\frac{d\hat{u}}{d\sigma} = \zeta\hat{v} - h_B'(x), \quad \text{and} \tag{17}$$

$$\frac{d\hat{v}}{d\sigma} = -\zeta\hat{u}, \tag{18}$$

subject to the (northern) boundary conditions

$$x|_{\sigma=0} = \mu, \tag{19}$$

$$\zeta|_{\sigma=0} = \zeta_0 \equiv \frac{\varepsilon^{1/3} + (\kappa\varepsilon)^{1/3}}{2(\kappa\varepsilon)^{1/3}} = \frac{1 + \kappa^{1/3}}{2\kappa^{1/3}} = 2.5, \tag{20}$$

$$\hat{h}|_{\sigma=0} = \frac{\zeta_0 h_0[\tilde{\tau}(\mu)]}{\sin y_0}, \tag{21}$$

$$\hat{u}|_{\sigma=0} = \frac{[h_B'(\mu)]^2}{\zeta_0^4}, \quad \text{and} \tag{22}$$

$$\hat{v}|_{\sigma=0} = \frac{h_B'(\mu)}{\zeta_0}, \tag{23}$$

where $-1 \le \mu \le 1$ is the coordinate across the characteristic curves and gives a parametric representation of the boundary data curve along $\zeta = \zeta_0$ and σ is the coordinate along the characteristics. The parameter μ only varies from -1 to $+1$ since for μ outside this range $\hat{h}|_{\sigma=0} = 0$ from (21).

The characteristics will be the curves $\mu = \hat{\mu}(x, \zeta)$ for which μ is a constant. To numerically compute the characteristics, it is necessary to ''start'' the solution at a finite value of ζ. The choice of ζ_0 in (20) corresponds, formally, to a value that is ''outside'' the inner equatorial region but ''inside'' the intermediate equatorial region. The qualitative behavior of the numerical solution is not sensitive to the particular choice of ζ_0.

The characteristic equations [(15)–(18)] are identical in form to the Lagrangian-particle initial-value model of Borisov and Nof (1998) used to investigate the trajectories of grounded abyssal eddies on an equatorial β plane in a meridional channel with parabolic bottom topography. The Borisov and Nof (1998) solutions show trajectories that initially meander about the equator subsequently developing into either ''chaotic'' or ''nonchaotic'' solutions depending on the magnitude of the parameter δ in $h_B'(x)$. The nonchaotic trajectories either eventually completely cross the equator and move poleward in the opposite hemisphere or ultimately return to the source hemisphere and move back poleward in the source hemisphere—in both cases on the eastern side of the channel. Kim et al. (2014) have recently shown that whether or not the trajectories eventually completely cross the equator is solely determined by the phase of the stationary planetary equatorial wave that the trajectory is in at the point of maximum eastward extent in the sense that if the meridional velocity is negative at the point of maximum eastward extent, the trajectories will eventually find themselves in the Southern Hemisphere, and in the Northern Hemisphere if the meridional velocity is positive at the point of maximum eastward extent. Whether the meridional velocity is negative or positive at the point of maximum eastward extent is solely determined by the position of the point of maximum eastward extent relative to the crest and trough of the stationary planetary equatorial wave yet to be described.

For the ''typical'' parameter values assumed here, the characteristic curves we obtain as solutions to (15)–(18) subject to (19)–(23) will exhibit complete cross-equatorial flow. In addition, we are able, under a suitable subapproximation (to be described later), to explicitly determine the wavelength of the stationary equatorial wave our solutions possess and the point of maximum eastward extent for each characteristic.

Moreover, we show that the characteristic curves intersect (i.e., formally a shock forms) within the stationary

planetary equatorial wave. Associated with this shock region $\nabla\hat{u}$ and $\nabla\hat{v}$ become unbounded (while u and v remain bounded). It is in this region of intersecting characteristics that dissipation makes a dominate contribution to the dynamics and acts to smooth out the sharp gradients in $\nabla\hat{u}$ and $\nabla\hat{v}$. That is, we argue that it is in these regions of intersecting characteristics that nonconservative or dissipative potential vorticity adjustment occurs, allowing cross-equatorial flow and the subsequent emergence of a geostrophically balanced topographically steered grounded DWBC in the opposite hemisphere.

Before moving on with our analysis, we comment that Chen and Byron-Scott (1995) have presented a Lagrangian-particle initial-value model for the cross-equatorial flow associated with the Asian–Australian monsoon. Unlike the Borisov and Nof (1998) model, the Chen and Byron-Scott (1995) model does not have a fixed pressure gradient in the *zonal* direction but rather a fixed pressure gradient in the *meridional* direction. This difference allows the Chen and Byron-Scott (1995) model to be explicitly solved in terms of elliptic functions for selected forms of the meridional pressure gradient. The Borisov and Nof (1998) model (and ours) has no explicit solution for $h'_B(x)$ given by (12) in Part I. We show, however, that under a suitable subapproximation, it is possible to explicitly solve our characteristic equations. Finally, we point out that in the purely inertial limit [i.e., set $h'_B(x) = 0$ in (17) but allow $\hat{u}|_{\sigma=0}$ and $\hat{v}|_{\sigma=0}$ to remain nonzero], it is possible to solve the characteristic equations (15)–(18) in terms of elliptic functions (Cushman-Roisin 1982), including their extension to spherical coordinates (Paldor and Killworth 1988; Pennell and Seitter 1990). Because there is no analytical solution to (15)–(18) for our choice of $h'_B(x)$, we will numerically solve the characteristic equations.

We note that (15)–(18) can be reduced to the coupled pair of equations

$$\frac{d^2}{d\sigma^2}(\hat{u} - \zeta^2/2) + \nu\delta\hat{u} = 0, \quad \text{and} \tag{24}$$

$$\frac{d^2\zeta}{d\sigma^2} + \hat{u}\zeta = 0, \tag{25}$$

which are not solvable in terms of elementary functions, except in a suitable subapproximation that will be described later. Equation (24) is the derivative along the characteristics of the angular momentum equation [see (27) below], and (25) is just the meridional momentum equation [(18)].

Another important property is that the characteristic equations conserve energy along the characteristics, since it follows from (15), (17), and (18) that

$$\frac{d}{d\sigma}\left[\frac{\hat{u}^2 + \hat{v}^2}{2} + \frac{h_B(x)}{\nu}\right] = 0$$

$$\Rightarrow \frac{\hat{u}^2 + \hat{v}^2}{2} + \frac{h_B(x)}{\nu} = \frac{[h'_B(\mu)]^4}{2\zeta_0^8} + \frac{[h'_B(\mu)]^2}{2\zeta_0^2} + \frac{h_B(\mu)}{\nu}, \tag{26}$$

where $(\hat{u}^2 + \hat{v}^2)/2$ is the kinetic energy and $h_B(x)/\nu$ is the gravitational potential energy. Since $h_B(x) \geq 0$, it follows from (26) that the inner equatorial region solutions necessarily have the property that the velocities are bounded. This is important because it means the singularities (as the equator is approached) associated with the intermediate region solutions are resolved in the inner equatorial region.

In addition, since $h''_B = \delta > 0$ and $h_B(\delta^{-1}) = h'_B(\delta^{-1}) = 0$, it follows from (26) that the maximum eastward extent of the characteristics must be finite. Note that energy conservation (26) [and (22) and (23)] also implies that in the flat bottom case, that is, h_B being a constant, the solutions are trivial in the sense that $\hat{u} = \hat{v} \equiv 0$. Sloping topography is therefore necessary for the flow within the inner equatorial region in the context of our model.

Finally, it is noted that angular momentum (Cushman-Roisin 1982) is not conserved along the characteristics since it follows from (16) and (17) that

$$\frac{d}{d\sigma}(\hat{u} - \zeta^2/2) = -h'_B(x) = 1 - \delta x. \tag{27}$$

Consequently, as the flow moves eastward, angular momentum increases along the characteristics for $x < 1/\delta$ (the western side of the channel) and decreases for $x < 1/\delta$ (the eastern side of the channel).

b. *Description of the numerical solution to the characteristic equations*

Figure 1a shows the pathlines or characteristic curves $[\hat{x}(\mu, \sigma), \hat{\zeta}(\mu, \sigma)]$ where $x = \hat{x}(\mu, \sigma)$ and $\zeta = \hat{\zeta}(\mu, \sigma)$ are the (numerically determined using *Mathematica*) solutions to (15) and (16) subject to (19) and (20), that is, $\hat{x}(\mu, 0) = \mu$ and $\hat{\zeta}(\mu, 0) = \zeta_0$, respectively, for $\mu = -1.0$ (black contour), -0.5 (blue contour), 0.0 (green contour), 0.5 (brown contour), and 1.0 (red contour), respectively, in the region $-2.5 \leq \zeta \leq 2.5$. Ignoring for the moment the fact that the characteristics are intersecting (on which we will comment further later), Fig. 1a shows the flow turning eastward as the inner equatorial region is entered, overshooting the equator (because of inertia) and subsequently turning back northward (because of the planetary vorticity gradient, as shown later). As the flow begins to turn northward the spread in the characteristics narrows (and indeed they intersect), and thereafter the spread in the characteristics increases

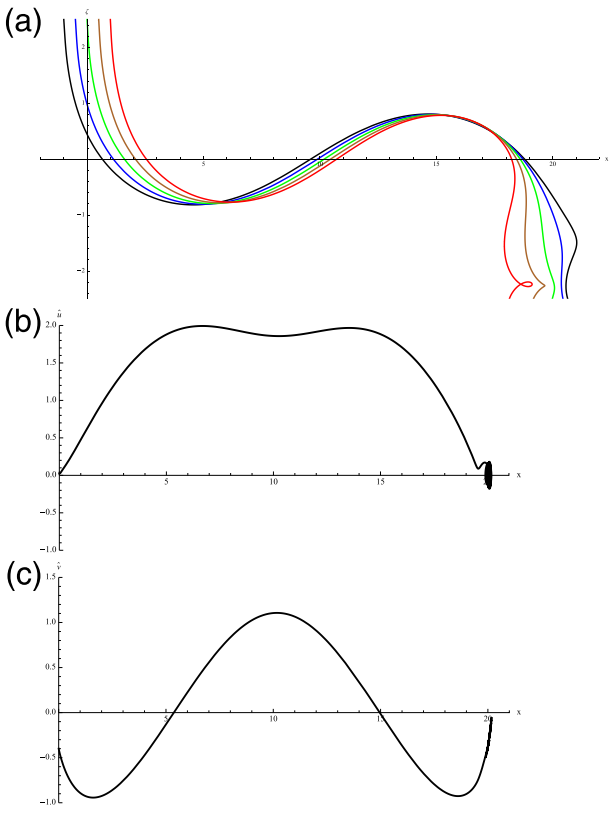

FIG. 1. (a) The characteristic curves $[\hat{x}(\mu, \sigma), \hat{\zeta}(\mu, \sigma)]$ for $\mu = -1.0, -0.5, 0.0, 0.5$ and 1.0. (b) The eastward velocity $\hat{u}(\mu, \sigma)$ vs x along the $\mu = 0$ characteristic. (c) The northward velocity $\hat{v}(\mu, \sigma)$ vs x along the $\mu = 0$ characteristic.

somewhat and it again overshoots the equator, subsequently turning back southward, where the spread in the characteristics decreases again (and they intersect again). By this point the flow is moving eastward and up the slope on the eastern side of the channel domain. Once the maximum eastward position is obtained, the zonal velocity decreases, the southward meridional velocity increases and the flow develops into an along-slope grounded abyssal current that is flowing southward in the Southern Hemisphere on the eastern side of the channel. The characteristic curves shown in Fig. 1a are qualitatively very similar to the Southern-to-Northern Hemisphere particle paths shown in Fig. 6a in Borisov and Nof (1998) when reflected through the equator.

Figures 1b and 1c show graphs of the zonal and meridional velocities $\hat{u}(\mu, \sigma)$ and $\hat{v}(\mu, \sigma)$ versus x along the $\mu = 0$ characteristic, respectively. The $\mu = 0$ characteristic is associated with the midpoint of the upstream DWBC where the thickness is maximum [see (21)]. It is important to emphasize that Figs. 1b and 1c are only meant to be understood qualitatively. In the regions where the characteristics intersect the formal solutions, $\hat{u}(\mu, \sigma)$ and $\hat{v}(\mu, \sigma)$ become multivalued (but nevertheless remain bounded) and as a result do not correspond to "classical" solutions to (8) and (9). Within the regions of intersecting characteristics, dissipation [not included in (8) and (9)] acts to smooth out the velocity field, resulting in a well-defined velocity field. Even with a smoothed velocity field, the flow would generally follow the path, qualitatively at least, like that shown in Fig. 1a.

Thus, with due consideration to the above cautionary comments, what can be surmised from Figs. 1b and 1c is that the inner inertial equatorial boundary layer has resulted in bounded velocities (i.e., removes the singularity in the asymptotic behavior in the intermediate region solutions), and this regularization occurs predominately because of inviscid processes, which allows the flow to move eastward, meandering along the equator until the eastern side of the channel domain is reached. The equatorial oscillations seen in the pathlines in Fig. 1a are very similar to those seen in the numerical simulations of Borisov and Nof (1998) and Kim et al. (2014). In the next section we will compute an explicit approximate formula for the "wavelength" of these equatorial planetary oscillations, and the result will be consistent with the oceanographic observations described in Part I.

The "squiggle" seen in Fig. 1b for $\hat{u}(\mu, \sigma)$ on the eastern side of the domain near $x \simeq 20$ is a consequence of the cross-slope oscillations seen in Fig. 1a as the flow exits the inner inertial boundary layer and moves ultimately southward along the topographic slope in the Southern Hemisphere [these oscillations can also be seen in the particle paths described in Borisov and Nof (1998)]. There are similar squiggles for $\hat{v}(\mu, \sigma)$ that are barely detectable in Fig. 1c near $x \simeq 20$, but these are small in comparison with the mean value $\hat{v}(\mu, \sigma) \simeq -0.4$ that occurs in the more or less geostrophically adjusted flow on the eastern side of the domain in the Southern Hemisphere. We do not ascribe physical significance to these oscillations, as they occur where the flow has exited the inner inertial equatorial boundary layer region and the computed solutions begin to lose asymptotic validity.

c. *The intersection of the pathlines or characteristic curves*

The pathlines or characteristics (both words are used interchangeably) begin to intersect when the Jacobian associated with the transformation from the Cartesian coordinates (x, ζ) to the characteristic coordinates (σ, μ) is zero, that is, when

$$\partial(\mu, \sigma) \equiv \hat{x}_\sigma \hat{\zeta}_\mu - \hat{x}_\mu \hat{\zeta}_\sigma = \nu \hat{u} \hat{\zeta}_\mu - \hat{v} \hat{x}_\mu = 0, \qquad (28)$$

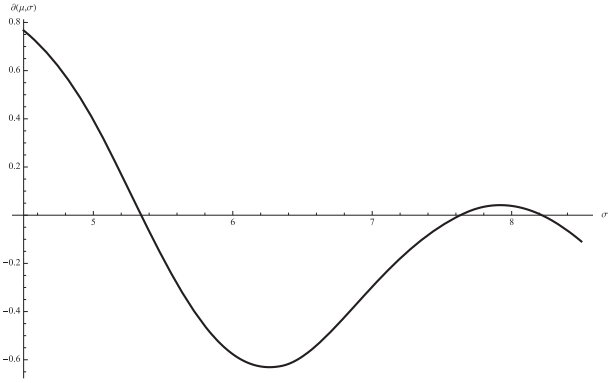

FIG. 2. A graph of the Jacobian $\partial(\mu, \sigma)$ for $\mu = 0$ for $4.5 \le \sigma \le 8.5$.

where (16) and (17) have been used. When the Jacobian is zero the transformation $x = \hat{x}(\mu, \sigma)$ and $\zeta = \hat{\zeta}(\mu, \sigma)$ is no longer invertible.

Figure 2 is a graph of the Jacobian $\partial(\mu, \sigma)$ for $\mu = 0$ for $4.5 \le \sigma \le 8.5$. The graphs for other values of μ are similar. [The derivatives $\hat{x}_\mu$ and $\hat{\zeta}_\mu$ in (28) were numerically computed using second-order accurate {i.e., $O[(\Delta\mu)^2]$} centered or one-sided as needed finite differences with $\Delta\mu = 10^{-5}$ over the interval $-1 \le \mu \le 1$.] The first zero, located near $\sigma \approx 5.4$ in Fig. 2, is associated with the intersecting characteristics in Fig. 1a located near $x \approx 5$ (in the "trough" of the stationary planetary equatorial wave). The second and third zeros, located near $\sigma \approx 7.6$ and 8.2, respectively, in Fig. 2, are associated with intersecting characteristics that occur in the "crest" of the stationary planetary equatorial wave located near $x \approx 16$ in Fig. 1a.

Figures 3a and 3b give a close-up view of selected characteristics curves $[\hat{x}(\mu, \sigma), \hat{\zeta}(\mu, \sigma)]$ near the zeros of $\partial(0, \sigma)$, as shown in Fig. 2, respectively. Figure 3a shows $[\hat{x}(\mu, \sigma), \hat{\zeta}(\mu, \sigma)]$ for $\mu = -1.0, -0.5, 0.0, 0.5$, and 1.0 in the region $4.9 \le x \le 6.6$ (with the same contour color scheme as in Fig. 1a). Figure 3b shows $[\hat{x}(\mu, \sigma), \hat{\zeta}(\mu, \sigma)]$ for $\mu = -1.0$ (black contour) and 1.0 (red contour) in the region $15 \le x \le 18$. A restricted set of characteristic curves is shown Fig. 3b in order to prevent unwanted "crowding" of the curves. Figure 3a shows the development of intersecting characteristics near $x \approx 5.1$ within the "trough" region in the stationary planetary equatorial wave as shown in Fig. 1a. In Fig. 3b we see, however, the formation of two regions with intersecting characteristics, with the first located near $x \approx 15.5$ and another near $x \approx 17.3$, but both are located within the "crest" region in the stationary equatorial wave as shown in Fig. 1a.

Based on Fig. 3a, one can estimate that the first region of intersecting characteristics is contained in the region $4.91 \lesssim x \lesssim 6.56$ and $-0.81 \lesssim \zeta \lesssim -0.76$. This corresponds, dimensionally, to a region that extends about

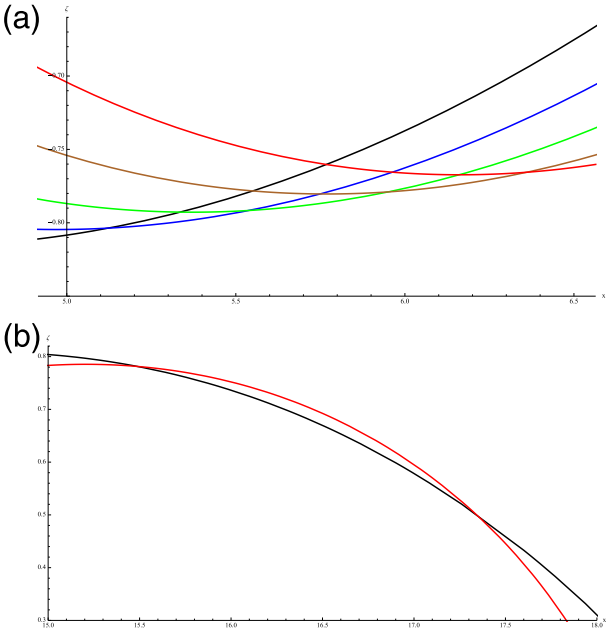

FIG. 3. (a) The characteristic curves $(\hat{x}, \hat{\zeta})$ for $\mu \in \{-1.0, -0.5, 0.0, 0.5, 1.0\}$ in $4.9 \le x \le 6.6$. (b) The characteristic curves $(\hat{x}, \hat{\zeta})$ for $\mu = -1.0$ and 1.0 in $15 \le x \le 18$.

165 and 11 km in the zonal and meridional directions, respectively. This is a zonally elongated and comparatively meridionally narrow region. The second and third regions of intersecting characteristics are even more zonally and meridionally constrained. Since the regions where the characteristics intersect will correspond to the regions where dissipation will be enhanced, this suggests that the dominate dissipative adjustment of the DWBC in the equatorial region occurs in a relatively small number of small area regions along the equator that are located near the crest and trough of the stationary planetary equatorial wave.

We argue, based on energy and geometrical considerations, that there must always be at least one region of intersecting characteristics within the stationary planetary equatorial wave (associated with genuine sustained cross-equatorial flow), and if there is more than one region of intersecting characteristics, there must always be an odd number of them.

In the purely inertial limit, it follows from energy conservation, that is, (26), that the maximum eastward extent, that is, the x coordinate, of the characteristics is finite. As will be shown below for an approximate model of the stationary equatorial wave, the maximum eastward position of a fluid parcel on the eastern side of the channel is symmetrically placed (about $x = 1/\delta$, the point of maximum depth) with respect to its initial upslope position on the western side of the channel. If the maximum

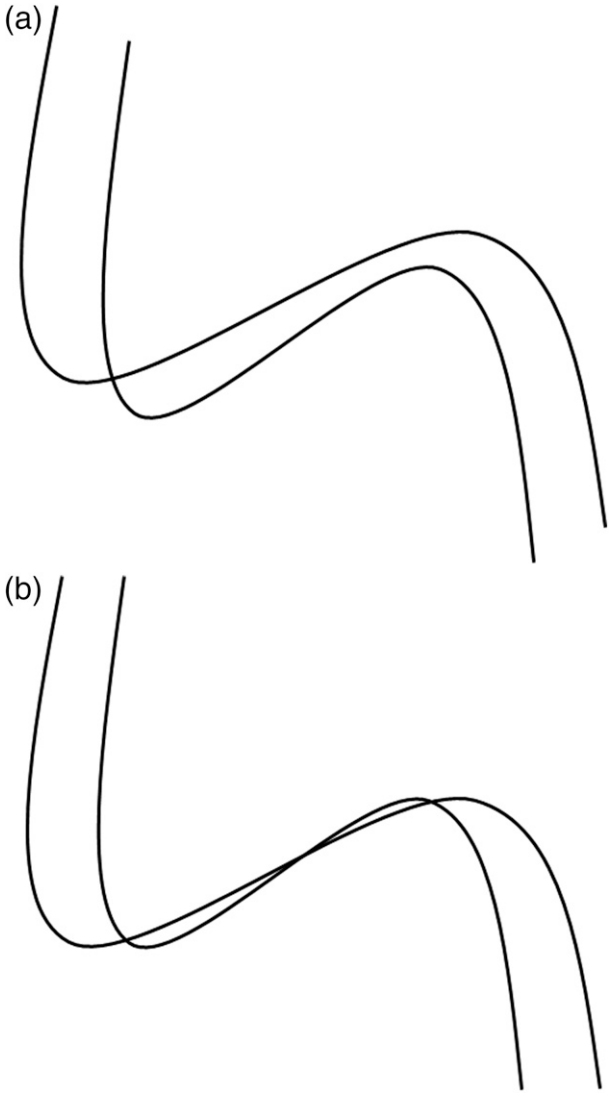

FIG. 4. (a) Idealized case where the upslope and downslope groundings possess a single crossing. (b) Idealized case where the upslope and downslope groundings possess a triple crossing.

eastward position of a fluid parcel on a pathline was further upslope, for example, than its position on the western slope, then the gravitational potential energy of the fluid parcel on the eastern side of the domain would exceed its gravitational potential energy on the western side and this would violate energy conservation (all else being equal) along the pathline.

The above scenario suggests that one should expect that the downslope (or upslope) grounding in the DWBC on the western side of the domain should map to the downslope (or upslope) grounding on the eastern side of the domain. Such a geometrical configuration can only occur, for genuine cross-equatorial flow, if there is an odd number of crossings of the pathlines associated with the downslope and upslope groundings. It is precisely at these crossings or intersections that the requisite dissipation happens, allowing nonconservative PV adjustment, which in turns permits the sustained cross-equatorial flow of a grounded DWBC that in midlatitudes is in planetary geostrophic balance.

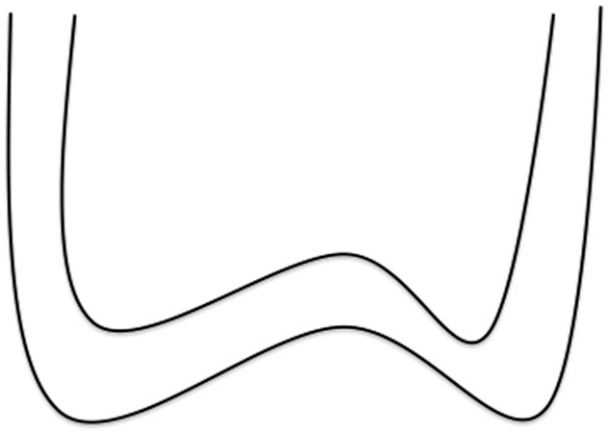

FIG. 5. Idealized case where the upslope and downslope groundings do not cross.

In Figs. 4a and 4b we show a hypothetical illustration of the single intersection case for the upslope and downslope groundings and the next possibility, which corresponds to the numerical solution obtained here, the triple intersection case, respectively. Clearly, the pattern in which the upslope (downslope) grounding on the western bank in the Northern Hemisphere maps to the upslope (downslope) grounding on the eastern bank in the Southern Hemisphere can only occur, for cross-equatorial flow, if there are an odd number of intersections.

On the other hand, if sustained cross-equatorial flow does not occur and the DWBC returns to the originating hemisphere (as it can do for certain parameter values; see Borisov and Nof 1998; Kim et al. 2014) then, consistent with the above physical argument, the pathlines need not intersect and, of course, no dissipation need occur. The simplest such case is illustrated in Fig. 5, which shows a hypothetical situation for a DWBC that approaches the equator on the western side, oscillates about the equator, and returns back to northern latitudes along the eastern side for which the upslope and downslope groundings do not intersect. It is emphasized that while the characteristics need not intersect in this scenario, if the pathlines did intersect, then they must do so an even number of times.

In the regions where the pathlines are intersecting, the velocity components $\hat{u}$ and $\hat{v}$ are finite, but the horizontal shear in the velocity becomes very large. The spatial gradients $\nabla\hat{u}$ and $\nabla\hat{v}$ are given, after a little algebra, by

$$\hat{u}_x = \hat{u}_\mu \mu_x + \hat{u}_\sigma \sigma_x = \frac{[\zeta\hat{v} - h_B'(x)]\hat{\zeta}_\mu - \hat{v}\hat{u}_\mu}{\partial(\mu,\sigma)}, \quad (29)$$

$$\hat{u}_\zeta = \hat{u}_\mu \mu_\zeta + \hat{u}_\sigma \sigma_\zeta = \frac{\nu\hat{u}\hat{u}_\mu - [\zeta\hat{v} - h_B'(x)]\hat{x}_\mu}{\partial(\mu,\sigma)}, \quad (30)$$

$$\hat{v}_x = \hat{v}_\mu \mu_x + \hat{v}_\sigma \sigma_x = -\frac{\zeta\hat{u}\hat{\zeta}_\mu + \hat{v}\hat{v}_\mu}{\partial(\mu,\sigma)}, \quad \text{and} \quad (31)$$

$$\hat{v}_\zeta = \hat{v}_\mu \mu_\zeta + \hat{v}_\sigma \sigma_\zeta = \frac{\nu\hat{u}\hat{v}_\mu + \zeta\hat{u}\hat{x}_\mu}{\partial(\mu,\sigma)}. \quad (32)$$

Consequently, when $\partial(\mu, \sigma) = 0$, the gradients $\nabla\hat{u}$ and $\nabla\hat{v}$ become unbounded and the $O(\mathrm{Re}^{-1})$ dissipative terms in (5) and (6) cannot be neglected in (8) and (9).

That is, in the regions where the pathlines are intersecting, (8) and (9) are replaced with

$$(\nu\hat{u}\partial_x + \hat{v}\partial_\zeta)\hat{u} - \zeta\hat{v} = -h_B'(x) + \frac{1}{\mathrm{Re}}(\nu^2\partial_{xx} + \partial_{\zeta\zeta})\hat{u}, \quad \text{and} \quad (33)$$

$$(\nu\hat{u}\partial_x + \hat{v}\partial_\zeta)\hat{v} + \zeta\hat{u} = -\kappa\hat{h}_\zeta + \frac{1}{\mathrm{Re}}(\nu^2\partial_{xx} + \partial_{\zeta\zeta})\hat{v}, \quad (34)$$

which corresponds to a pair of coupled nonlinear elliptic equations. It is beyond the scope of this paper to fully solve (33) and (34), and this is left for another submission. It is noted that Borisov and Nof (1998) and Kim et al. (2014) have numerically solved the full (initial value) shallow-water equations with dissipation included for the cross-equatorial flow of a grounded DWBC on parabolic bottom topography. In the near-equatorial region, their solutions for the pathlines are qualitatively very similar to that shown in Fig. 1a with, however, the gradients "smoothed" out so that velocity field remains continuously differentiable in the pathline intersecting regions as shown in Fig. 1a.

Figures 6a and 6b show graphs of $\hat{u}_x$ and $\hat{v}_x$, respectively, versus x along the $\mu = 0$ characteristic for the range $0 \le x \lesssim 5.74$ [the x coordinate associated with the shock point where $\partial(0, \sigma) = 0$]. The graphs for $\hat{u}_x$ and $\hat{v}_x$ along other characteristics and the graphs for $\hat{u}_y$ and $\hat{v}_y$ are qualitatively similar. We see that both $\hat{u}_x$ and $\hat{v}_x$ are relatively constant over much of the interval until the shock point is reached, at which they rapidly become singular. Finally, we note that since $x = 1$ corresponds, dimensionally, to about 200 km, it follows that $x \simeq 5.74$ corresponds to a point that is about 1048 km east of the initial downslope grounding associated with the DWBC in midlatitudes. Hence, the theory presented here suggests that the DWBC flows inertially quite a distance zonally along the equator before dissipation sets in.

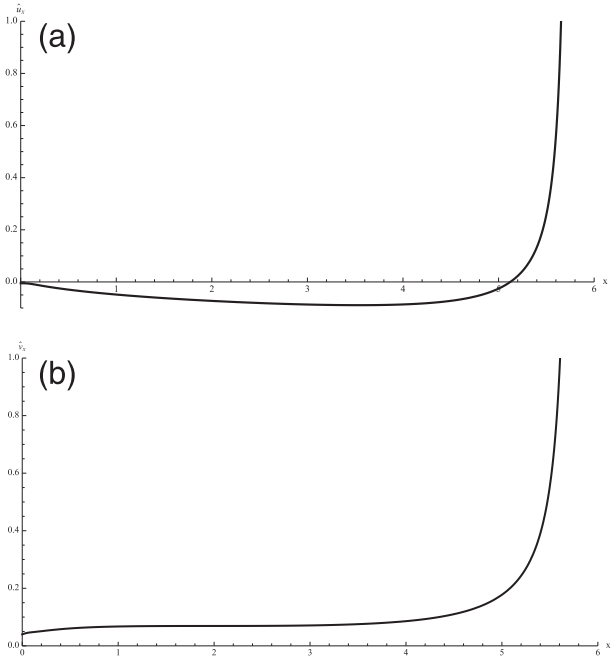

FIG. 6. (a) Graph of $\hat{u}_x$ vs x along the $\mu = 0$ characteristic. (b) Graph of $\hat{v}_x$ vs x along the $\mu = 0$ characteristic.

The ζ coordinate varies as one moves along the $\mu = 0$ characteristic, and by the time the shock point is approached the flow has entered the Southern Hemisphere (see Fig. 1a). In the interval $0 \le x \lesssim 1.61$, the flow along the $\mu = 0$ characteristic is in the Northern Hemisphere, and in the interval $1.61 \lesssim x \lesssim 5.74$, the flow along the $\mu = 0$ characteristic is in the Southern Hemisphere (see Fig. 1a). The inner region solutions for u and v have eliminated the singular behavior associated with the intermediate and midlatitude solutions as the equator is approached so that they remain bounded as the equator is crossed. Unfortunately, the resulting bounded solutions for the velocities possess singularities in the velocity gradients as the shock region is approached, which is rectified by dissipation.

The solution for $\hat{h}$ in the inner region is most conveniently obtained from the PV equation [(14)], which in characteristic coordinates is given by

$$\left(\frac{\nu\hat{v}_x - \hat{u}_\zeta + \zeta}{\hat{h}}\right)_\sigma = 0, \quad (35)$$

which is solved subject to (21). The inner solutions conserve the PV along the characteristics. The solution for $\hat{h}$ can therefore be written in the form

$$\hat{h} = \left(\frac{\hat{h}}{\nu\hat{v}_x - \hat{u}_\zeta + \zeta}\right)_{\sigma=0} (\nu\hat{v}_x - \hat{u}_\zeta + \zeta), \quad (36)$$

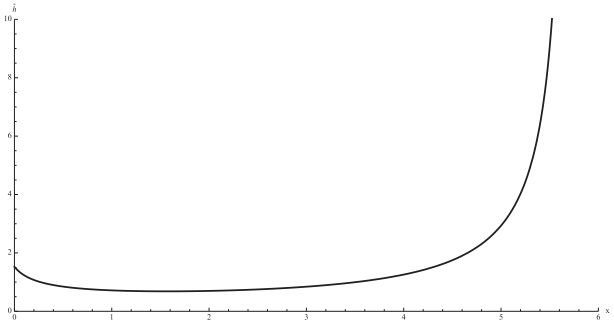

FIG. 7. Graph of $\hat{h}$ vs x along the $\mu = 0$ characteristic.

where $\hat{v}_x$ and $\hat{u}_\zeta$ are given by (29) and (32), respectively. Figure 7 shows a graph of $\hat{h}$ versus x along the $\mu = 0$ characteristic for the range $0 \le x \le 5.74$. The graphs for $\hat{h}$ along other characteristics are qualitatively similar. As the flow moves along the characteristics, we see an initial decrease in $\hat{h}$ as x increases (i.e., the equator is being approached) consistent with the asymptotic behavior predicted by the midlatitude and intermediate equatorial region solutions. However, the inner solution possesses the property that the height is no longer decreasing to zero as the equator is crossed. The height becomes unbounded as the region where the pathlines are intersecting is entered and dissipation can no longer be ignored.

3. An approximate model for the stationary equatorial wave

It is possible to introduce an approximation into the characteristic equations [(15)–(18)] that permits an analytical solution for the inviscid problem in the inner equatorial region. To our knowledge, the nonlinear steady-state solution we present here has not appeared before in the literature. Examination of Fig. 1a suggests that within the stationary equatorial wave ζ and $\hat{v}$ are "small" in comparison to $\hat{u}$ and that, based on (16), ζ and $\hat{v}$ are comparable in magnitude. This suggests that the Coriolis term $\zeta\hat{v}$ can be neglected in the zonal momentum equation [(17)], resulting in the approximate set of "inner" characteristic equations

$$\frac{dx}{d\sigma} = \nu u, \tag{37a}$$

$$\frac{d\zeta}{d\sigma} = v, \tag{37b}$$

$$\frac{du}{d\sigma} = 1 - \delta x, \quad \text{and} \tag{38a}$$

$$\frac{dv}{d\sigma} = -\zeta u, \tag{38b}$$

subject to the boundary conditions

$$x|_{\sigma=0} = \mu, \quad \zeta|_{\sigma=0} = \zeta_0, \quad \text{and} \tag{39}$$

$$u|_{\sigma=0} = u_0(\mu) \equiv \frac{[h_B'(\mu)]^2}{\zeta_0^4}, \quad v|_{\sigma=0} = v_0(\mu) \equiv \frac{h_B'(\mu)}{\zeta_0}, \tag{40}$$

where, for convenience and to avoid confusion with the numerical solution to the full set of equations presented previously, we have, again, dropped the carets.

Energy conservation along the characteristics associated with this approximate model is given by

$$\frac{d}{d\sigma}\left[\frac{\hat{u}^2}{2} + \frac{h_B(x)}{\nu}\right] = 0 \Rightarrow \frac{\hat{u}^2}{2} + \frac{h_B(x)}{\nu} = \frac{[h_B'(\mu)]^4}{2\zeta_0^8} + \frac{h_B(\mu)}{\nu}.$$

As in the full model, since $h_B'' = \delta > 0$ and $h_B(\delta^{-1}) = h_B'(\delta^{-1}) = 0$, it follows from energy conservation that the maximum eastward extent of the characteristics must be finite.

Physically, (38a) implies that the zonal velocity is determined, to leading order, by a balance between nonlinear advection and the gravitational acceleration associated with the topographic gradient (i.e., a classical steady one-dimensional downslope gravity current). Mathematically, neglecting the Coriolis term $\zeta\hat{v}$ in (17) allows x and u to be obtained without reference to ζ and v and that ζ and v will be obtained subsequently with u determined.

Equations (37a) and (38a) imply that

$$\frac{d^2u}{d\sigma^2} + \delta\nu u = 0, \tag{41}$$

which will be solved subject to

$$u|_{\sigma=0} = u_0(\mu) \quad \text{and} \quad \left.\frac{du}{d\sigma}\right|_{\sigma=0} = 1 - \delta\mu, \tag{42}$$

and (37b) and (38b) imply that

$$\frac{d^2\zeta}{d\sigma^2} + u\zeta = 0, \tag{43}$$

which will be solved subject to

$$\zeta|_{\sigma=0} = \zeta_0 \quad \text{and} \quad \left.\frac{d\zeta}{d\sigma}\right|_{\sigma=0} = v_0(\mu), \tag{44}$$

with x and v determined by

$$x = \frac{1}{\delta}\left(1 - \frac{du}{d\sigma}\right) \quad \text{and} \quad v = \frac{d\zeta}{d\sigma}. \tag{45}$$

The solution to (41), which satisfies (42), can be written in the form

$$u(\mu,\sigma)=\alpha(\mu)\cos[\sqrt{\delta\nu}\sigma-\theta(\mu)], \tag{46}$$

where

$$\alpha(\mu)\equiv\sqrt{u_0^2(\mu)+\frac{(1-\delta\mu)^2}{\delta\nu}},\quad \theta(\mu)\equiv\arctan\left(\frac{1-\delta\mu}{u_0(\mu)\sqrt{\delta\nu}}\right). \tag{47}$$

It follows from (45) that

$$x(\mu,\sigma)=[1+\alpha\sqrt{\delta\nu}\sin(\sqrt{\delta\nu}\sigma-\theta)]/\delta. \tag{48}$$

If (46) is substituted into (43), one obtains the Mathieu equation (Abramowitz and Stegun 1970)

$$\frac{d^2\zeta}{d\sigma^2}+\alpha\cos(\sqrt{\delta\nu}\sigma-\theta)\zeta=0, \tag{49}$$

the solution of which [which satisfies (44)] can be written in the form

$$\zeta(\mu,\sigma)=A(\mu)C\left(0,-\frac{2\alpha}{\delta\nu},\frac{\sqrt{\delta\nu}\sigma-\theta}{2}\right)+B(\mu)S\left(0,-\frac{2\alpha}{\delta\nu},\frac{\sqrt{\delta\nu}\sigma-\theta}{2}\right), \tag{50}$$

with

$$A(\mu)\equiv\frac{2v_0S\left(0,-\frac{2\alpha}{\delta\nu},-\frac{\theta}{2}\right)-\zeta_0\sqrt{\delta\nu}S'\left(0,-\frac{2\alpha}{\delta\nu},-\frac{\theta}{2}\right)}{\sqrt{\delta\nu}W(\mu)}, \tag{51}$$

$$B(\mu)\equiv\frac{\zeta_0\sqrt{\delta\nu}C'\left(0,-\frac{2\alpha}{\delta\nu},-\frac{\theta}{2}\right)-2v_0C\left(0,-\frac{2\alpha}{\delta\nu},-\frac{\theta}{2}\right)}{\sqrt{\delta\nu}W(\mu)}, \text{ and} \tag{52}$$

$$W(\mu)\equiv S\left(0,-\frac{2\alpha}{\delta\nu},-\frac{\theta}{2}\right)C'\left(0,-\frac{2\alpha}{\delta\nu},-\frac{\theta}{2}\right)-S'\left(0,-\frac{2\alpha}{\delta\nu},-\frac{\theta}{2}\right)C\left(0,-\frac{2\alpha}{\delta\nu},-\frac{\theta}{2}\right), \tag{53}$$

where $C(a, q, \tau)$ and $S(a, q, \tau)$ are the fundamental Mathieu cosine and sine solutions, respectively, of the generic Mathieu equation

$$y_{\tau\tau}+[a-2q\cos(2\tau)]y=0,$$

(Abramowitz and Stegun 1970) and prime means differentiation with respect to the third argument. It follows from (45) that

$$v(\mu,\sigma)=\frac{\sqrt{\delta\nu}}{2}\left[A(\mu)C'\left(0,-\frac{2\alpha}{\delta\nu},\frac{\sqrt{\delta\nu}\sigma-\theta}{2}\right)+B(\mu)S'\left(0,-\frac{2\alpha}{\delta\nu},\frac{\sqrt{\delta\nu}\sigma-\theta}{2}\right)\right]. \tag{54}$$

It is possible to explicitly determine the maximum eastward extent of the flow along each characteristic for these solutions. The maximum eastward extent of the flow occurs when $u = 0$, and this occurs, from (46), for $\sqrt{\delta\nu}\sigma-\theta(\mu)=\pi/2$, which, when substituted into (48), implies that the maximum eastward extent, or run-up point on the upsloping bottom topography on the eastern side of the basin, denoted by $x_{\max}(\mu)$, is given by

$$x_{\max}(\mu)=\frac{1+\sqrt{\delta\nu u_0^2(\mu)+(1-\delta\mu)^2}}{\delta}. \tag{55}$$

The maximum eastward extent $x_{\max}(\mu)$ varies very little with respect to μ with $x_{\max}(1)\simeq 19$ and $x_{\max}(-1)\simeq 21$, or about $2/\delta = 20$ units to the east from the initial position, that is, symmetrically placed about the point of maximum depth. The maximum eastward run-up point of the flow associated with the upslope grounding in the current on the western side of the basin is farther eastward, that is, more upslope, than the maximum eastward run-up point of the flow associated with the downslope grounding in the current on the western side of the basin. This follows since the gravitational potential energy of the flow associated with the downslope grounding on the western side of the basin is less than the gravitational potential energy of the flow associated with the upslope grounding on the western side of the basin.

Figure 8a shows the characteristic curves $[x(\mu, \sigma), \zeta(\mu, \sigma)]$, where $x = x(\mu, \sigma)$ and $\zeta = \zeta(\mu, \sigma)$ are given by (48) and (50), respectively, for $\mu = -1.0$ (black contour), -0.5 (blue contour), 0.0 (green contour), 0.5 (brown contour), and 1.0 (red contour) in the region $-2.5 \le \zeta \le 2.5$. Figure 8a is qualitatively very similar to (and reproduces the stationary wave pattern in) the numerical solution to the full characteristic equations shown in Fig. 1a, except right along the eastern boundary where the characteristics in Fig. 1a exit the inner equatorial region, that is, where the Coriolis terms can no longer be neglected in the zonal momentum equation.

Figures 8b and 8c show graphs of the zonal and meridional velocities $u(\mu, \sigma)$ and $v(\mu, \sigma)$ versus x along the $\mu = 0$ characteristic, respectively. The graphs associated with other characteristics are qualitatively similar. It is noted that the solutions for x and u given by (46) and (48), respectively, imply that the curve seen in Fig. 8b corresponds to a portion of the ellipse given by

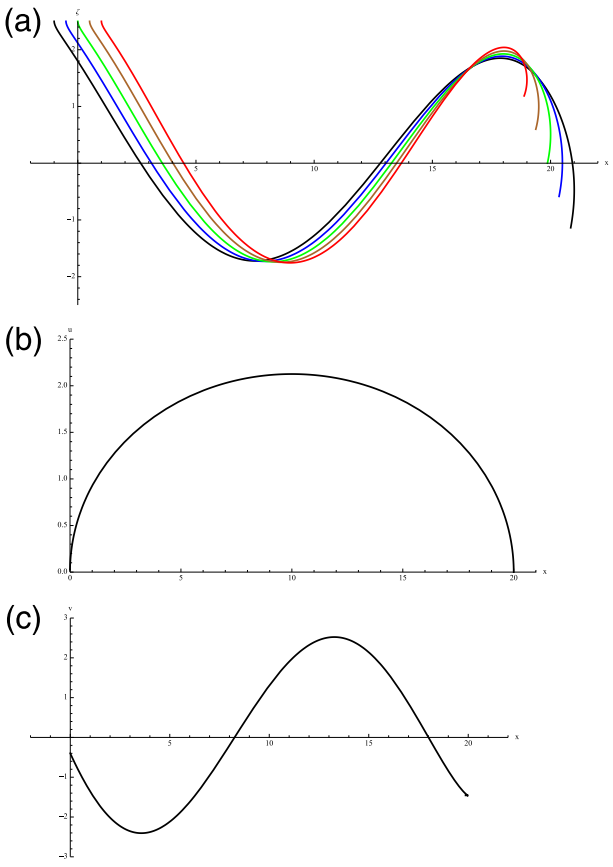

FIG. 8. (a) The characteristic curves $[x(\mu,\sigma), \zeta(\mu,\sigma)]$ for $\mu = -1.0, -0.5, 0.0, 0.5$ and 1.0. (b) The eastward velocity $u(\mu,\sigma)$ vs x along the $\mu = 0$ characteristic. (c) The northward velocity $v(\mu,\sigma)$ vs x along the $\mu = 0$ characteristic.

$$\frac{(\delta x - 1)^2}{\delta\nu} + u^2 = \alpha^2 .$$

Figures 8b and 8c are to be compared with Figs. 1b and 1c, respectively, which show the related graphs for the numerical solution to the full characteristic equations. Again, qualitatively, the approximate solution derived here reproduces the large-scale structure associated with the numerical solution to the full characteristic equations.

It is important to emphasize again that Figs. 8a–c are only meant to be understood only very qualitatively. In the regions where the characteristics intersect (see Fig. 8a) the formal solutions $u(\mu,\sigma)$ and $v(\mu,\sigma)$ become multivalued (but nevertheless remain bounded) and as a result do not correspond to classical solutions to the underlying equations. Within the regions of intersecting characteristics, dissipation acts to smooth out the velocity field result in a well-defined velocity field. Nevertheless, the inviscid approximate solutions depicted in Figs. 8a–c describe, qualitatively, the large-scale planetary equatorial wave within the inner equatorial region rather well. Finally, we do not show solutions for the DWBC height associated with this approximate model because it becomes singular in the regions of intersecting characteristics.

While it is possible to numerically determine the "wavelength" of the equatorial planetary wave using the Mathieu function solution [(50)], a simpler, explicit, and accurate representation can be obtained as follows. Observe that over the physically relevant interval for the stationary planetary wave $0 \le \sqrt{\delta\nu}\sigma - \theta \le \pi/2$ that $\cos(\sqrt{\delta\nu}\sigma - \theta)$ monotonically decreases from 1 to 0. This suggests replacing $\cos(\sqrt{\delta\nu}\sigma - \theta)$ in (43) with its average positive value over the interval $0 \le \sqrt{\delta\nu}\sigma - \theta \le \pi/2$, which is given by $2/\pi$, that is, we approximate (43) with

$$\frac{d^2\zeta}{d\sigma^2} + \frac{2\alpha}{\pi}\zeta = 0, \tag{56}$$

the solution of which [which satisfies (44)] is given by

$$\zeta = \varphi(\mu)\cos[\sqrt{2\alpha(\mu)/\pi}\sigma - \psi(\mu)], \tag{57}$$

where

$$\varphi(\mu) \equiv \sqrt{\zeta_0^2 + \pi v_0^2/(2\alpha)}, \quad \psi(\mu) \equiv \arctan\left(\frac{v_0}{\zeta_0\sqrt{2\alpha/\pi}}\right). \tag{58}$$

We can obtain an approximate solution of the form $\zeta = \zeta(x)$ by eliminating σ in (57) using the inverse relation obtained from (48), given by

$$\sigma = \hat{\sigma}(x) \equiv \frac{1}{\sqrt{\delta\nu}}\left[\theta + \arcsin\left(\frac{\delta x - 1}{\alpha\sqrt{\delta\nu}}\right)\right], \tag{59}$$

which describes σ as a function of x along each characteristic μ = constant.

Finally, if (59) is substituted into (57) we have, along each characteristic, that

$$\zeta(x) = \varphi\cos\left(\left\{\sqrt{2\alpha/(\delta\nu\pi)}\left[\theta + \arcsin\left(\frac{\delta x - 1}{\alpha\sqrt{\delta\nu}}\right)\right] - \psi\right\}\right). \tag{60}$$

The solution [(60)] describes a stationary planetary equatorial wave with amplitude φ and a "wavelength" over the first cycle, denoted as λ, given by

$$\lambda = \frac{1 + (\delta\mu - 1)\cos(\sqrt{2\nu\delta\pi^3/\alpha}) + u_0\sqrt{\delta\nu}\sin(\sqrt{2\nu\delta\pi^3/\alpha})}{\delta}. \tag{61}$$

As derived, (61) is independent of the specific details of the abyssal velocity profile entering the inner equatorial region in that it depends quite generically on the "initial" values u_0 and v_0, which need not necessarily be those determined by the μ dependence given in (40) (which *is* set by the specific form of the current as it exits the intermediate region). Thus, λ as determined by (61) would be a generic estimate for the wavelength of the equatorial wave regardless of the particular form of the midlatitude solution.

As an example, the wavelength associated with the $\mu = 0$ characteristic would be $\lambda|_{\mu=0} \simeq 18.3$, which dimensionally corresponds to a zonal wavelength of about 1830 km, which is qualitatively consistent with the oceanographic observations and numerical simulations. The wavelengths for other physical values of μ (i.e., $-1 \le \mu \le 1$) are very similar. Figure 9 shows a graph of $\zeta = \zeta(x)$ as described by (61) for the $\mu = 0$ characteristic for the interval $0 \le x \le 20$. Comparing Fig. 9 with the green ($\mu = 0$) characteristic in Fig. 8a, we see that, qualitatively, the approximate solution [(60)] faithfully reproduces, for the most part, the Mathieu function solution. The graphs associated with other physical values of μ are very similar to those shown in Fig. 8a.

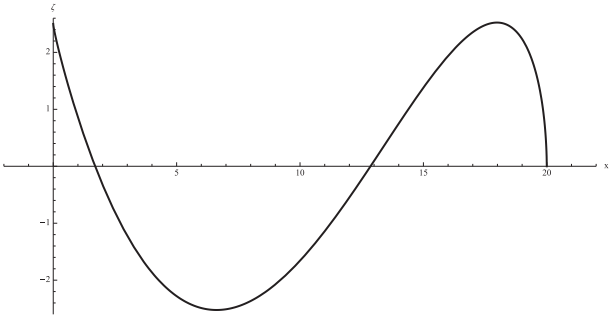

FIG. 9. Graph of $\zeta = \zeta(x)$ given by (60) for $\mu = 0$ for the interval $0 \le x \le 20$.

4. Conclusions

A comprehensive theoretical study of the nonlinear cross-equatorial steady-state dynamics of a grounded DWBC has been given. The spatial domain considered was a differentially rotating meridionally aligned basin with zonally varying parabolic bottom topography so that the model ocean shallows on both the western and eastern sides of the basin.

As shown in Part I, away from the equator the flow was shown to be governed by a nonlinear planetary geostrophic balance in which the potential vorticity equation can be explicitly solved. The flow in midlatitudes exhibits increasing speed as the flow approaches the equator with the DWBC height decreasing (as a consequence of PV conservation). The midlatitude flow maintains constant meridional volume transport with respect to latitude. In addition, there is a slight upslope transport induced in midlatitudes as the flow moves equatorward, which arises because of the planetary vorticity gradient.

As the flow enters the equatorial region, it becomes increasingly nonlinear and passes through two distinguished inertial boundary layers, which are referred to as the "intermediate" and "inner" inertial equatorial regions, respectively. In Part I the flow in the intermediate region was explicitly determined. For typical parameter values, the meridional scale of the intermediate region corresponds to about 885 km centered on the equator. Within the so-called intermediate region, the flow accelerates eastward as it flows equatorward, eventually becoming predominately zonal. The DWBC thickness continues to decrease as the intermediate region is traversed. This unphysical behavior is finally resolved in the inner equatorial region. For typical parameter values, the outer boundary of the inner region corresponds to a distance of about 221 km from the equator. The structure of the flow in this inner equatorial region was the subject of this paper.

The large-scale structure of the flow within the inner equatorial region corresponds to a zonally aligned stationary planetary wave pattern that meanders about the equator in which the flow ultimately exits the equatorial region on the eastern side of the basin along the sloping eastern boundary. If the DWBC exits the equatorial region into the opposite hemisphere from its source hemisphere, it was shown that the characteristics or pathlines of the flow must necessarily intersect within the inner inertial equatorial boundary layer. The velocity within the inner equatorial region is shown to be finite everywhere (the singular behavior associated with the midlatitude and intermediate regions is resolved), but in the regions of intersecting characteristics, the velocity becomes multivalued and the horizontal velocity gradients become infinite. In addition, it is shown that the DWBC height or thickness, which is determined from potential vorticity conservation, becomes infinite in the regions of intersecting characteristics (because the relative vorticity becomes singular). It is at these regions that dissipation makes a leading-order contribution to the dynamics and induces the requisite potential vorticity adjustment permitting the cross-equatorial flow of DWBC that in midlatitudes is in planetary geostrophic balance.

In addition, an approximate nonlinear inviscid model was introduced for the zonally aligned stationary equatorial planetary wave pattern that meanders about the equator within the inner equatorial region that could be

analytically solved. In particular, it is possible to explicitly determine the maximum eastern extent of the flow and the wavelength of the planetary wave (on the order of 1830 km) before it exits the inner equatorial region on the eastern side of the basin. The approximate model does a very good job of reproducing the large-scale structure of the stationary planetary wave pattern along the equator consistent with the available observations (which are described in Part I).

Acknowledgments. Preparation of this manuscript was supported in part by Discovery Grants awarded by the Natural Sciences and Engineering Research Council (NSERC) of Canada.

REFERENCES

Abramowitz, M., and I. A. Stegun, 1970: *Handbook of Mathematical Functions*. 9th ed. Dover, 1041 pp.

Borisov, S., and D. Nof, 1998: Deep, cross-equatorial eddies. *Geophys. Astrophys. Fluid Dyn.*, **87**, 273–310, doi:10.1080/03091929808221150.

Chen, T. S., and R. A. D. Byron-Scott, 1995: Bifurcation in cross-equatorial airflow: A nonlinear characteristic of Lagrangian modeling. *J. Atmos. Sci.*, **52**, 1383–1400, doi:10.1175/1520-0469(1995)052<1383:BICEAA>2.0.CO;2.

Cushman-Roisin, B., 1982: Motion of a free particle on a beta-plane. *Geophys. Astrophys. Fluid Dyn.*, **22**, 85–102, doi:10.1080/03091928208221738.

Edwards, C. A., and J. Pedlosky, 1998a: Dynamics of nonlinear cross-equatorial flow. Part I: Potential vorticity transformation. *J. Phys. Oceanogr.*, **28**, 2382–2406, doi:10.1175/1520-0485(1998)028<2382:DONCEF>2.0.CO;2.

——, and ——, 1998b: Dynamics of nonlinear cross-equatorial flow. Part II: The tropically enhanced instability of the western boundary current. *J. Phys. Oceanogr.*, **28**, 2407–2417, doi:10.1175/1520-0485(1998)028<2407:DONCEF>2.0.CO;2.

Kim, A., G. E. Swaters, and B. R. Sutherland, 2014: Cross-equatorial flow of grounded abyssal ocean currents. *Geophys. Astrophys. Fluid Dyn.*, **108**, 363–386, doi:10.1080/03091929.2014.891023.

Paldor, N., and P. D. Killworth, 1988: Inertial trajectories on a rotating Earth. *J. Atmos. Sci.*, **45**, 4013–4019, doi:10.1175/1520-0469(1988)045<4013:ITOARE>2.0.CO;2.

Pennell, S. A., and K. L. Seitter, 1990: On inertial motion on a rotating sphere. *J. Atmos. Sci.*, **47**, 2032–2034, doi:10.1175/1520-0469(1990)047<2032:OIMOAR>2.0.CO;2.

Swaters, G. E., 2015: Midlatitude-equatorial dynamics of a grounded deep western boundary current. Part I: Midlatitude flow and the transition to the equatorial region. *J. Phys. Oceanogr.*, **45**, 2457–2469, doi:10.1175/JPO-D-14-0207.1.